Flavor-violating Higgs and top decays in the type 1B flavorful two-Higgs-doublet model with a twist

Ti-Bin Hou,[1,2,3,*] Zheng Li,[1,2,3] Yu-Ju Peng,[1,2,3] Jin-Lei Yang,[1,2,3,†] Hao-Ran Ma,[1,2,3] and Tai-Fu Feng[1,2,3,4,‡]

[1]*Department of Physics, Hebei University, Baoding 071002, China*

[2]*Hebei Key Laboratory of High-precision Computation and Application of Quantum Field Theory, Baoding 071002, China*

[3]*Hebei Research Center of the Basic Discipline for Computational Physics, Baoding 071002, China*

[4]*Department of Physics, Chongqing University, Chongqing 401331, China*

(Received 18 July 2026; accepted 31 August 2026; published 25 September 2026)

We study flavor-violating decays of the SM-like Higgs boson and rare top decays in the type 1B realization of the flavorful two-Higgs-doublet model with a twist, focusing on $h \to sb$, $h \to db$, $h \to uc$, $h \to \mu\tau$, $h \to e\tau$, $h \to e\mu$, $t \to ch$, and $t \to uh$. We present the relevant amplitude and branching-ratio formulae, include one-loop vertex corrections, and impose constraints from Higgs signal-strength measurements, electroweak precision tests, meson mixing, $B \to X_s\gamma$, direct HFV searches, and CLFV constraints, including $\mu - e$ conversion. The surviving parameter space favors $\mathrm{BR}(h \to sb) \gg \mathrm{BR}(h \to db)$, $\mathrm{BR}(t \to ch) \gg \mathrm{BR}(t \to uh)$, and $\mathrm{BR}(h \to \mu\tau) \gg \mathrm{BR}(h \to e\tau) \sim \mathrm{BR}(h \to e\mu)$ in the lepton sector. One-loop effects usually preserve these hierarchies, but can modify individual channels through different mechanisms: sizable destructive tree-loop interference can reduce $h \to sb$ enough to yield rare $\mathrm{BR}_{1\mathrm{L}}(h \to db) > \mathrm{BR}_{1\mathrm{L}}(h \to sb)$ points, whereas the large relative corrections found in rare top decays mainly reflect strong SM-like alignment suppressing the tree-level amplitudes.

DOI: 10.1103/l8qz-q978

I. INTRODUCTION

The discovery of the Higgs boson by ATLAS and CMS Collaborations completed the particle content of the Standard Model (SM), leaving the observed pattern of fermion masses and flavor mixing as an open question [1,2]. Higgs interactions therefore remain a direct probe of the flavor puzzle. In a generic two-Higgs-doublet model (2HDM), the presence of several Yukawa matrices leads to tree-level flavor-changing neutral currents (FCNCs). The traditional solution is natural flavor conservation, in which each fermion species couples to only one scalar doublet [3,4]. Yukawa alignment provides another well-known way to suppress scalar FCNCs [5]. These ideas underlie much of the conventional 2HDM classification and phenomenology [6].

The absence of large observed FCNCs is compatible with a structured scalar flavor sector. Controlled scalar flavor violation can arise if the nonstandard Yukawa couplings are correlated with fermion masses and mixing. Early examples include the Cheng-Sher ansatz and top-specific scalar flavor violation [7–9]. Branco-Grimus-Lavoura constructions provide another important class in which scalar FCNC couplings are controlled by Cabibbo-Kobayashi-Maskawa (CKM) matrix elements [10–12]. These examples motivate extended Higgs sectors with structured flavor violation.

Flavorful two-Higgs-doublet models follow this philosophy. The flavor-locked flavorful 2HDM showed that characteristic Higgs signatures can be compatible with flavor data when the Yukawa sector is organized by a controlled flavor structure [13]. The flavorful two-Higgs-doublet model with a twist introduced several twisted Yukawa realizations, including the type 1B case studied here [14]. The Type 1B flavorful two-Higgs-doublet model (F2HDM) has a nonstandard flavor structure, approximate protection of first-second generation transitions, and in the implementation considered here a CKM matrix generated in the down sector, distinguishing it from the ordinary natural-flavor-conserving type I 2HDM.

The experimental situation makes Higgs and top-flavor violation especially relevant. Direct LHC searches for charged-lepton-flavor-violating Higgs decays have reached subpercent sensitivity in $h \to \mu\tau$ and $h \to e\tau$, while $h \to e\mu$ is constrained even more strongly [15–17]. Charged-lepton flavor violation in heavy-particle decays, including Higgs, Z, and top decays, is a broad probe of new flavor

*Contact author: 3078849770@qq.com
†Contact author: jlyang@hbu.edu.cn
‡Contact author: fengtf@hbu.edu.cn

Published by the American Physical Society under the terms of the Creative Commons Attribution 4.0 International license. Further distribution of this work must maintain attribution to the author(s) and the published article's title, journal citation, and DOI. Funded by SCOAP³.

dynamics [18]. Top-Higgs FCNC interactions are likewise well motivated because SM top-FCNC branching fractions are extremely small [19]. Top-FCNC decays have also been analyzed in several $U(1)$-extended BSM frameworks, including flavor-dependent $U(1)$ and $B-L$-type models [20,21]. LHC searches for $t \to Hq$ in $H \to b\bar{b}$, $H \to \gamma\gamma$, and multilepton final states now probe branching fractions at the per-mille level or below [22–24].

On the theory side, Higgs flavor violation has been studied in effective-coupling approaches, general 2HDMs, aligned 2HDMs, and flavorful Higgs frameworks [25–30]. Collider signatures of flavorful Higgs bosons can differ substantially from those of natural-flavor-conserving 2HDMs [31]. Rare top decays have also been proposed as direct probes of flavorful Higgs sectors [32]. Related flavor-dependent Higgs-sector studies have investigated rare Higgs decays, top-FCNC channels, charged-lepton-flavor violation, and electroweak precision constraints in $U(1)_F$-type models [33]. These studies provide the context for a joint numerical analysis of Higgs and top-flavor violation in a type 1B F2HDM.

In this work we analyze the channels $h \to sb$, $h \to db$, $h \to uc$, $h \to \mu\tau$, $h \to e\tau$, $h \to e\mu$, $t \to ch$, and $t \to uh$, using the charge-conjugate convention specified below. The final sample is obtained after Higgs, electroweak, flavor, and low-energy selections. The numerical results identify $h \to sb$, $t \to ch$, $h \to db$, and $h \to \mu\tau$ as the leading channels in the numerical setup used here, reveal a structured flavor pattern, and show that the down-sector Higgs FCNC rates are much more stable at tree level than the texture- and alignment-sensitive tree-level $t \to ch$ and $h \to \mu\tau$ modes. We also examine one-loop vertex effects in Higgs-mediated FCNC decays and rare top decays.

The paper is organized as follows. Section II describes the type 1B F2HDM. Section III defines the observables and numerical procedure. Section IV presents the numerical results. Section V gives the conclusions.

II. THE TYPE 1B F2HDM

We work in the type 1B realization of the flavorful two-Higgs-doublet model with a twist [14]. This model is different from the ordinary natural-flavor-conserving type I two-Higgs-doublet model. In the type 1B F2HDM, the two scalar doublets have a nonstandard flavor assignment: Φ_1 gives the dominant contribution to fermion masses of the first two generations, whereas Φ_2 gives fermion masses dominantly of the third generation. Consequently, the two doublets couple to different fermion species dominantly, and tree-level flavor-changing neutral Higgs couplings are generically present.

The type 1B assignment used here is

	u	d	ℓ
First two generations	Φ_1	Φ_1	Φ_1
Third generation	Φ_2	Φ_2	Φ_2

(1)

understood as a texture assignment distinct from a natural-flavor-conserving zero pattern. The small entries controlled by the approximate $U(2)^5$ flavor structure and by the $O(1)$ coefficients populate both doublets in a way that reproduces fermion masses and the CKM matrix.

A. Scalar sector

The scalar sector contains two scalar doublets $\Phi_a \sim (2,+1/2)$ under $SU(2)_L \times U(1)_Y$,

$$\Phi_a = \begin{pmatrix} \phi_a^+ \\ \frac{v_a+\rho_a+i\eta_a}{\sqrt{2}} \end{pmatrix}, \qquad a = 1,2, \tag{2}$$

with

$$v^2 = v_1^2 + v_2^2, \qquad \tan\beta = \frac{v_2}{v_1}. \tag{3}$$

We restrict the scalar sector to the commonly used charge-parity (CP)-conserving softly broken Z_2-type scalar-potential form. The Z_2 breaking is retained only through the quadratic soft term m_{12}^2, while the hard-breaking quartic terms are not included. The scalar potential is

$$\begin{aligned} V(\Phi_1,\Phi_2) = {} & m_{11}^2\Phi_1^\dagger\Phi_1 + m_{22}^2\Phi_2^\dagger\Phi_2 - [m_{12}^2\Phi_1^\dagger\Phi_2 + \text{H.c.}] \\ & + \lambda_1(\Phi_1^\dagger\Phi_1)^2 + \lambda_2(\Phi_2^\dagger\Phi_2)^2 \\ & + \lambda_3(\Phi_1^\dagger\Phi_1)(\Phi_2^\dagger\Phi_2) + \lambda_4(\Phi_2^\dagger\Phi_1)(\Phi_1^\dagger\Phi_2) \\ & + \left[\frac{\lambda_5}{2}(\Phi_2^\dagger\Phi_1)^2 + \text{H.c.}\right]. \end{aligned} \tag{4}$$

All scalar-potential parameters in Eq. (4) are taken real in the CP-conserving numerical implementation. The neutral CP-even states are obtained from

$$\begin{pmatrix} h \\ H \end{pmatrix} = Z^h \begin{pmatrix} \rho_1 \\ \rho_2 \end{pmatrix}, \tag{5}$$

with analogous rotations for the CP-odd and charged sectors. The reduced light-Higgs vector coupling is

$$\kappa_V \equiv \frac{g_{hVV}}{g_{hVV}^{\text{SM}}} = \frac{v_1 Z_{11}^h + v_2 Z_{12}^h}{v}. \tag{6}$$

The alignment preselection used below is expressed in terms of this quantity. The alignment-distance variable used in the plots is

$$|\cos(\beta-\alpha)| \equiv \sqrt{\max(0, 1-\kappa_V^2)},$$

which follows the convention $\kappa_V = \sin(\beta-\alpha)$ for an SM-like light Higgs. The sign of the soft term in Eq. (4) follows the project convention $-m_{12}^2(\Phi_1^\dagger\Phi_2 + \text{H.c.})$.

B. Yukawa Lagrangian and type 1B texture

The two-doublet notation used in this work is $\Phi_{1,2}$. In the mass-parameter notation of Ref. [14], the doublet associated with the dominant third-generation masses is denoted by ϕ, while the other doublet is denoted by ϕ'. For the type 1B assignment in Eq. (1), these conventions are related by

$$\phi \equiv \Phi_2, \qquad \phi' \equiv \Phi_1, \qquad v = v_2, \qquad v' = v_1,$$

and the corresponding Yukawa matrices are related by

$$\lambda^u = Y_2^u, \qquad \lambda^d = Y_2^d, \qquad \lambda^e = Y_2^\ell,$$
$$\lambda'^u = Y_1^u, \qquad \lambda'^d = Y_1^d, \qquad \lambda'^e = Y_1^\ell.$$

With $\tilde{\phi}^{(\prime)} = i\sigma_2(\phi^{(\prime)})^*$, the Yukawa part of the flavorful two-Higgs-doublet Lagrangian is written as

$$\begin{aligned} -\mathcal{L}_Y \supset & \sum_{i,j}[\lambda^u_{ij}(\bar{q}_i u_j)\tilde{\phi} + \lambda^d_{ij}(\bar{q}_i d_j)\phi + \lambda^e_{ij}(\overline{\ell}_i e_j)\phi + \text{H.c.}] \\ & + \sum_{i,j}[\lambda'^u_{ij}(\bar{q}_i u_j)\tilde{\phi}' + \lambda'^d_{ij}(\bar{q}_i d_j)\phi' \\ & + \lambda'^e_{ij}(\overline{\ell}_i e_j)\phi' + \text{H.c.}]. \end{aligned} \tag{7}$$

Together with the mapping above, Eq. (7) serves as the notation bridge between the ϕ, ϕ' mass-parameter convention and the Φ_1, Φ_2 texture notation used below.

The type 1B flavor assignment is represented by the following flavor-basis Yukawa textures. Up to independent $O(1)$ coefficients, the first doublet carries the light-generation texture, while the second doublet carries the rank-one third-generation texture [14]:

$$Y_1^u \sim \frac{\sqrt{2}}{v_1}\begin{pmatrix} m_u & m_u & m_u \\ m_u & m_c & m_c \\ m_u & m_c & m_c \end{pmatrix}, \quad Y_2^u \sim \frac{\sqrt{2}}{v_2}\begin{pmatrix} 0 & 0 & 0 \\ 0 & 0 & 0 \\ 0 & 0 & m_t \end{pmatrix} \tag{8}$$

$$Y_1^d \sim \frac{\sqrt{2}}{v_1}\begin{pmatrix} m_d & \lambda m_s & \lambda^3 m_b \\ m_d & m_s & \lambda^2 m_b \\ m_d & m_s & m_s \end{pmatrix}, \quad Y_2^d \sim \frac{\sqrt{2}}{v_2}\begin{pmatrix} 0 & 0 & 0 \\ 0 & 0 & 0 \\ 0 & 0 & m_b \end{pmatrix} \tag{9}$$

$$Y_1^\ell \sim \frac{\sqrt{2}}{v_1}\begin{pmatrix} m_e & m_e & m_e \\ m_e & m_\mu & m_\mu \\ m_e & m_\mu & m_\mu \end{pmatrix}, \quad Y_2^\ell \sim \frac{\sqrt{2}}{v_2}\begin{pmatrix} 0 & 0 & 0 \\ 0 & 0 & 0 \\ 0 & 0 & m_\tau \end{pmatrix}. \tag{10}$$

Here λ denotes the Cabibbo-sized expansion parameter in the down sector, and the symbol $\sim$ indicates the parametric texture form. The explicit scan uses independent coefficients O^u_{ij}, O^d_{ij}, and O^ℓ_{ij} to realize these textures while exactly reconstructing the physical fermion masses.

Using this mapping and rotating the fermions into mass eigenstates, we define

$$m^u_{qq'} = \frac{v}{\sqrt{2}}\langle q_L|\lambda^u|q'_R\rangle, \qquad m'^u_{qq'} = \frac{v'}{\sqrt{2}}\langle q_L|\lambda'^u|q'_R\rangle, \qquad q, q' = u, c, t, \tag{11}$$

$$m^d_{qq'} = \frac{v}{\sqrt{2}}\langle q_L|\lambda^d|q'_R\rangle, \qquad m'^d_{qq'} = \frac{v'}{\sqrt{2}}\langle q_L|\lambda'^d|q'_R\rangle, \qquad q, q' = d, s, b, \tag{12}$$

$$m^\ell_{\ell\ell'} = \frac{v}{\sqrt{2}}\langle \ell_L|\lambda^\ell|\ell'_R\rangle, \qquad m'^\ell_{\ell\ell'} = \frac{v'}{\sqrt{2}}\langle \ell_L|\lambda'^\ell|\ell'_R\rangle, \qquad \ell, \ell' = e, \mu, \tau. \tag{13}$$

In each charged-fermion sector these mass parameters obey $m^f_{ij} + m'^f_{ij} = m_{f_i}\delta_{ij}$. The charged-fermion texture coefficients are denoted as O^u_{ij}, O^d_{ij}, and O^ℓ_{ij}; the flavor label is a superscript and the matrix element is a subscript.

The explicit primed mass matrices $M'_f \equiv (m'^f_{ij})$ used to reconstruct the charged-fermion Yukawa sector are [14]

$$M'_u = \begin{pmatrix} m_u + O^u_{11}\frac{m_u^2}{m_t} & \frac{(O^u_{13}m_u)(O^u_{32}m_c)}{m_t}\left(1 + O^u_{12}\frac{m_c}{m_t}\right) & O^u_{13}m_u \\ \frac{(O^u_{23}m_c)(O^u_{31}m_u)}{m_t}\left(1 + O^u_{21}\frac{m_c}{m_t}\right) & m_c + O^u_{22}\frac{m_c^2}{m_t} & O^u_{23}m_c \\ O^u_{31}m_u & O^u_{32}m_c & O^u_{33}m_c \end{pmatrix}, \tag{14}$$

$$M'_d = \begin{pmatrix} m_d - O^d_{31}m_d V^*_{td}\left(1 + O^d_{11}\frac{m_s}{m_b}\right) & O^d_{32}m_s V^*_{td}\left(1 + O^d_{12}\frac{m_s}{m_b}\right) & -V^*_{td}m_b\left(1 + O^d_{13}\frac{m_s}{m_b}\right) \\ O^d_{31}m_d V^*_{ts}\left(1 + O^d_{21}\frac{m_s}{m_b}\right) & m_s - O^d_{32}m_s V^*_{ts}\left(1 + O^d_{22}\frac{m_s}{m_b}\right) & -V^*_{ts}m_b\left(1 + O^d_{23}\frac{m_s}{m_b}\right) \\ O^d_{31}m_d & O^d_{32}m_s & O^d_{33}m_s \end{pmatrix}, \tag{15}$$

$$M'_\ell = \begin{pmatrix} m_e + O^\ell_{11}\frac{m_e^2}{m_\tau} & \frac{(O^\ell_{13}m_e)(O^\ell_{32}m_\mu)}{m_\tau}\left(1 + O^\ell_{12}\frac{m_\mu}{m_\tau}\right) & O^\ell_{13}m_e \\ \frac{(O^\ell_{23}m_\mu)(O^\ell_{31}m_e)}{m_\tau}\left(1 + O^\ell_{21}\frac{m_\mu}{m_\tau}\right) & m_\mu + O^\ell_{22}\frac{m_\mu^2}{m_\tau} & O^\ell_{23}m_\mu \\ O^\ell_{31}m_e & O^\ell_{32}m_\mu & O^\ell_{33}m_\mu \end{pmatrix}. \tag{16}$$

Together with Eqs. (11)–(13), these matrices determine the Yukawa couplings used in the charged-fermion FCNC analysis.

In the numerical realization used below, the CKM matrix is generated in the down sector,

$$V_{Lu} \simeq I, \quad V_{Ru} \simeq I, \quad V_{Ld} \simeq V_{\rm CKM}, \quad V_{Rd} \simeq I. \tag{17}$$

Equation (17) is the basis choice and numerical ansatz used in the scan. The texture by itself does not fix this rotation pattern. With our fermion-rotation convention,

$$V_{\rm CKM} = V^\dagger_{Lu} V_{Ld}.$$

Thus $V_{Lu} \simeq I$ implies $V_{Ld} \simeq V_{\rm CKM}$, while $V_{Rd} \simeq I$ is an additional simplifying assumption. In this section we specify the type 1B texture and the corresponding mass-basis Yukawa definition. The conversion of these mass-basis matrices into the numerical input basis used for the scan is part of the numerical procedure.

III. OBSERVABLES AND NUMERICAL PROCEDURE

A. Decay channels and charge-conjugate convention

The numerical analysis considers the flavor-violating Higgs channels $h \to \mu\tau$, $h \to e\tau$, $h \to e\mu$, $h \to sb$, $h \to db$, and $h \to uc$, together with the top-FCNC channels $t \to ch$ and $t \to uh$.

Throughout the paper, the shorthand notation for neutral Higgs decays includes the charge-conjugate final states. We define

$$\mathrm{BR}(h \to sb) \equiv \mathrm{BR}(h \to s\bar{b}) + \mathrm{BR}(h \to \bar{s}b), \tag{18}$$

$$\mathrm{BR}(h \to db) \equiv \mathrm{BR}(h \to d\bar{b}) + \mathrm{BR}(h \to \bar{d}b), \tag{19}$$

$$\mathrm{BR}(h \to uc) \equiv \mathrm{BR}(h \to u\bar{c}) + \mathrm{BR}(h \to \bar{u}c), \tag{20}$$

and, for charged-lepton channels,

$$\mathrm{BR}(h \to \mu\tau) \equiv \mathrm{BR}(h \to \mu^-\tau^+) + \mathrm{BR}(h \to \mu^+\tau^-), \tag{21}$$

$$\mathrm{BR}(h \to e\tau) \equiv \mathrm{BR}(h \to e^-\tau^+) + \mathrm{BR}(h \to e^+\tau^-), \tag{22}$$

$$\mathrm{BR}(h \to e\mu) \equiv \mathrm{BR}(h \to e^-\mu^+) + \mathrm{BR}(h \to e^+\mu^-). \tag{23}$$

The same charge-conjugate convention is used when comparing tree-level and one-loop quantities for the quark channels.

B. Amplitudes and decay widths

For the quark-Higgs channels, we parametrize the amplitude in a chiral form-factor basis,

$$\mathcal{M}(h \to f_i\bar{f}_j) = \bar{u}_i(p_i)[G_L^{h,ij}P_L + G_R^{h,ij}P_R]v_j(p_j), \tag{24}$$

where $f_i\bar{f}_j = s\bar{b}, d\bar{b}, u\bar{c}$ for the explicitly calculated directions. The one-loop form factors are decomposed schematically as

$$G_X^{h,ij} = g_{X,\rm tree}^{h,ij} + \Delta g_{X,\rm tri}^{h,ij}, \qquad X = L, R, \tag{25}$$

where $\Delta g_{X,\rm tri}$ denotes the one-loop vertex contribution.

For top-FCNC decays, we use

$$\mathcal{M}(t \to q_i h) = \bar{u}_{q_i}(p_q)[G_L^{tq_i}P_L + G_R^{tq_i}P_R]u_t(p_t), \tag{26}$$

with

$$G_X^{tq_i} = g_{X,\rm tree}^{tq_i} + \Delta g_{X,\rm tri}^{tq_i}, \quad q_i = u, c, \quad X = L, R. \tag{27}$$

With this convention, the two-body decay width for a neutral scalar decay into two fermions is

$$\Gamma(h \to f_i\bar{f}_j) = \frac{N_c\lambda^{1/2}(m_h^2, m_i^2, m_j^2)}{16\pi m_h^3}[(m_h^2 - m_i^2 - m_j^2) \times (|G_L|^2 + |G_R|^2) - 4m_i m_j \mathrm{Re}(G_L G_R^*)], \tag{28}$$

where $N_c = 3$ for quark final states and $\lambda(x, y, z) = x^2 + y^2 + z^2 - 2xy - 2xz - 2yz$. The charge-conjugate branching ratio is

$$\mathrm{BR}(h \to f_i f_j) = \frac{\Gamma(h \to f_i\bar{f}_j) + \Gamma(h \to \bar{f}_i f_j)}{\Gamma_h^{\rm tot}}. \tag{29}$$

For the top decay in Eq. (26),

$$\Gamma(t \to q_i h) = \frac{\lambda^{1/2}(m_t^2, m_q^2, m_h^2)}{16\pi m_t^3}[(m_t^2 + m_q^2 - m_h^2)(|G_L|^2 + |G_R|^2) + 4m_t m_q \mathrm{Re}(G_L G_R^*)]. \tag{30}$$

The branching ratio is

$$\mathrm{BR}(t \to q_i h) = \frac{\Gamma(t \to q_i h)}{\Gamma_t^{\mathrm{tot}}}. \tag{31}$$

The total widths Γ_h^{tot} and Γ_t^{tot} are the widths used in the corresponding numerical normalization.

C. One-loop vertex corrections

For the explicitly calculated quark-Higgs and top-Higgs FCNC channels, we compare the tree-level amplitude with the one-loop vertex contribution shown by category in Figs. 1(a) and 2. We write the amplitude as

$$\mathcal{M}_{1\mathrm{L}} = \mathcal{M}_{\mathrm{tree}} + \mathcal{M}_{\mathrm{loop}}. \tag{32}$$

The corresponding rate-level expression is

$$\mathrm{BR}_{1\mathrm{L}} = \mathrm{BR}_{\mathrm{tree}} + \Delta\mathrm{BR}_{\mathrm{int}} + \mathrm{BR}_{\mathrm{loop}^2}, \tag{33}$$

where $\Delta\mathrm{BR}_{\mathrm{int}}$ is proportional to $2\mathrm{Re}(\mathcal{M}_{\mathrm{tree}}^{*}\mathcal{M}_{\mathrm{loop}})$, and $\mathrm{BR}_{\mathrm{loop}^2}$ is proportional to $|\mathcal{M}_{\mathrm{loop}}|^2$. We define

$$\delta_{1\mathrm{L}} \equiv \frac{\mathrm{BR}_{1\mathrm{L}} - \mathrm{BR}_{\mathrm{tree}}}{\mathrm{BR}_{\mathrm{tree}}}. \tag{34}$$

D. Parameter scan and constraints

The numerical scan uses the parameter ranges and preselection requirements summarized in Table I. The scalar sector is sampled in $\tan\beta$, m_{12}^2, and the quartic couplings $\lambda_{1,\ldots,5}$ appearing in Eq. (4). This softly broken Z_2-type scalar-potential choice removes hard Z_2-breaking quartic terms, reduces the number of independent scalar-sector parameters, and keeps the flavor nonuniversality studied here in the Yukawa texture rather than in additional scalar-potential structures. The scan further imposes an SM-like light-Higgs mass window, heavy non-SM scalar masses above the TeV scale, a charged-pseudoscalar mass-splitting requirement, and an alignment preselection before the full set of phenomenological constraints is applied.

We impose the following theoretical and phenomenological constraints in the numerical pipeline. Theoretical constraints on the scalar sector are imposed following the standard 2HDM perturbativity, tree-level unitarity, and bounded-from-below criteria, translated to the scalar-potential convention of Eq. (4) [6].

a. Perturbativity. The scalar quartic couplings are required to satisfy $\max|\lambda_i^{\mathrm{ref}}| < 4\pi$. The reconstructed Yukawa matrices are also required to remain perturbative, $\max|Y_{a,ij}^{f}| \le \sqrt{4\pi}$.

b. Tree-level scalar unitarity. The largest eigenvalue entering the scalar two-body scattering matrix is required to be smaller than 8π.

c. Bounded-from-below and vacuum stability. Our scalar potential uses $\lambda_1(\Phi_1^\dagger\Phi_1)^2 + \lambda_2(\Phi_2^\dagger\Phi_2)^2$, while the convention of Ref. [6] uses $(\lambda_1^B/2)(\Phi_1^\dagger\Phi_1)^2 + (\lambda_2^B/2)(\Phi_2^\dagger\Phi_2)^2$. The correspondence is $\lambda_1^B = 2\lambda_1$, $\lambda_2^B = 2\lambda_2$, while $\lambda_{3,4,5}^B = \lambda_{3,4,5}$ up to the harmless $\Phi_1^\dagger\Phi_2$ versus $\Phi_2^\dagger\Phi_1$ complex-conjugation convention. For the CP-conserving scalar potential in Eq. (4), the bounded-from-below conditions become

$$\begin{aligned} &\lambda_1 > 0, \qquad \lambda_2 > 0, \\ &\lambda_3 + 2\sqrt{\lambda_1\lambda_2} > 0, \qquad \lambda_3 + \lambda_4 - |\lambda_5| + 2\sqrt{\lambda_1\lambda_2} > 0. \end{aligned} \tag{35}$$

d. Higgs signal strengths. The Higgs signal-strength selection uses the global one-sigma condition

$$\Delta\chi^2_{\mathrm{HS}} \equiv \chi^2_{\mathrm{HS}} - \chi^2_{\mathrm{HS,min}} \le 1, \tag{36}$$

where χ^2_{HS} is the HiggsSignals chi-square and $\chi^2_{\mathrm{HS,min}}$ is the minimum value in the generated scan. Numerically, the 50000-point sample gives $\chi^2_{\mathrm{HS,min}} = 149.872$, so the applied cut is $\chi^2_{\mathrm{HS}} \le 150.872$.

e. Electroweak precision constraints. We require the obtained S, T, U values to lie within the current experimental 1σ ranges quoted in the Review of Particle Physics [34]:

$$\begin{aligned} &S = -0.04 \pm 0.10, \qquad T = 0.01 \pm 0.12, \\ &U = -0.01 \pm 0.09. \end{aligned} \tag{37}$$

The three intervals are applied independently in the numerical scan.

f. Neutral-meson mixing. Neutral-meson mixing constraints are imposed using the observable-specific two-sided 95% probability intervals reported in Table 3 of the model-independent analysis of Ref. [35]:

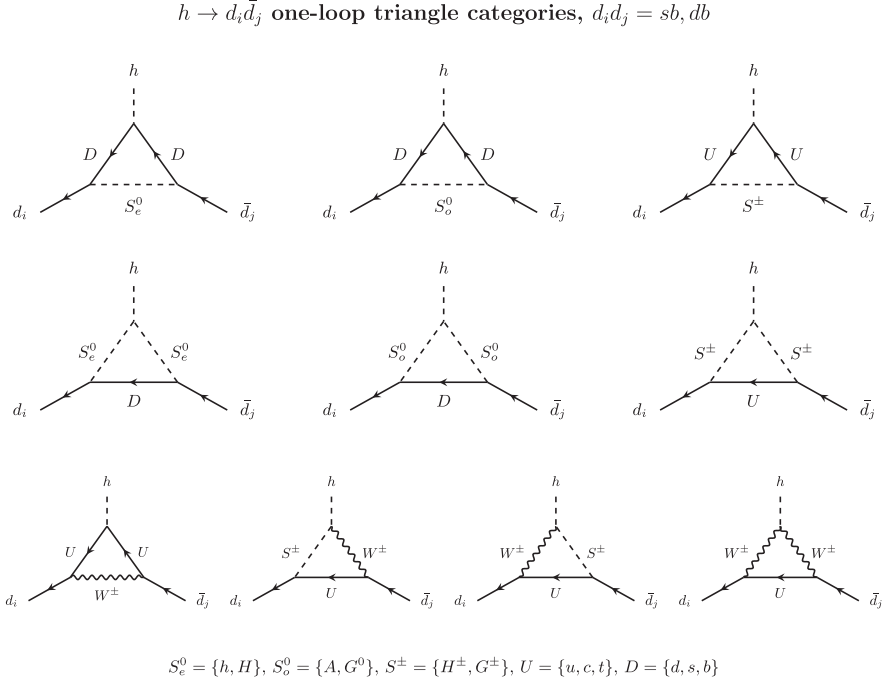
$$\begin{aligned} &0.63 \le \frac{\Delta M_{B_s}}{\Delta M_{B_s}^{\mathrm{SM}}} \le 2.07, \qquad 0.53 \le \frac{\Delta M_{B_d}}{\Delta M_{B_d}^{\mathrm{SM}}} \le 2.05, \\ &0.51 \le \frac{\Delta M_K}{\Delta M_K^{\mathrm{SM}}} \le 2.07, \qquad 0.66 \le \frac{\epsilon_K}{\epsilon_K^{\mathrm{SM}}} \le 1.31. \end{aligned} \tag{38}$$

The four conditions are applied independently. The B_s and B_d ratios constrain neutral-meson mixing in the $b \leftrightarrow s$ and $b \leftrightarrow d$ sectors, respectively, while ΔM_K and ϵ_K probe the dispersive and CP-violating components of K^0-$\bar{K}^0$ mixing. For ΔM_K, we use the short-distance ratio returned by FlavorKit rather than imposing the experimental mass-splitting uncertainty directly, owing to the sizable long-distance contribution to kaon mixing.

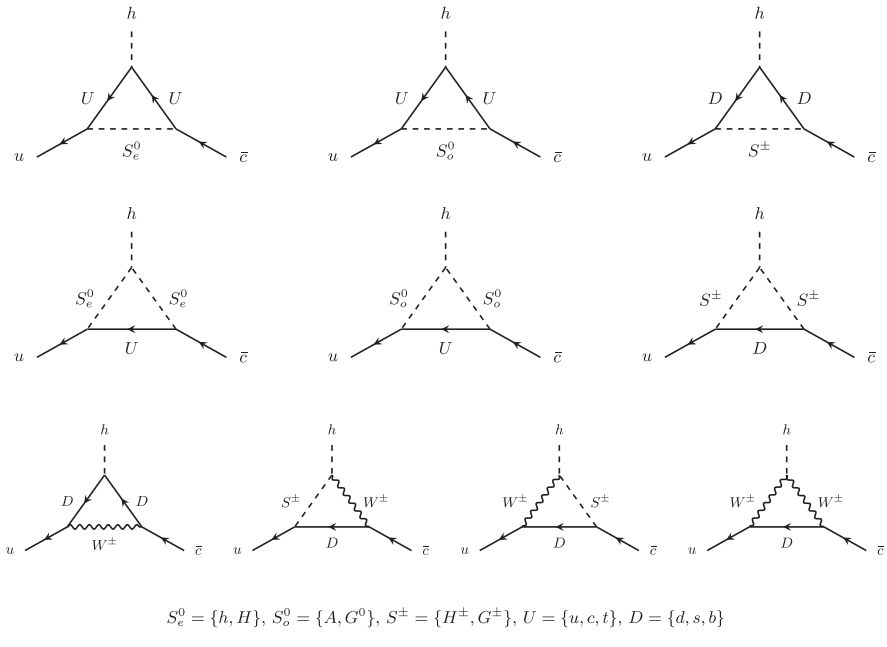
g. $B \to X_s\gamma$. The radiative B-decay constraint is imposed using the inclusive reference interval [36] as

$$2.99 \times 10^{-4} \le \mathrm{BR}(B \to X_s\gamma) \le 3.87 \times 10^{-4}. \tag{39}$$

h. Charged-lepton flavor and $\mu - e$ conversion constraints. The lepton-sector Higgs-flavor-violating (HFV) branching ratios are required to satisfy the current direct 95% C.L. limits



(a) Down-sector Higgs FCNC channels $h \to d_i \bar{d}_j$ with $d_i d_j = sb, db$.



(b) Up-sector Higgs FCNC channel $h \to u\bar{c}$.

FIG. 1. One-loop triangle categories for the Higgs FCNC channels. The notation is $S_e^0 = \{h, H\}$, $S_o^0 = \{A, G^0\}$, and $S^\pm = \{H^\pm, G^\pm\}$, with $U = \{u, c, t\}$ and $D = \{d, s, b\}$.

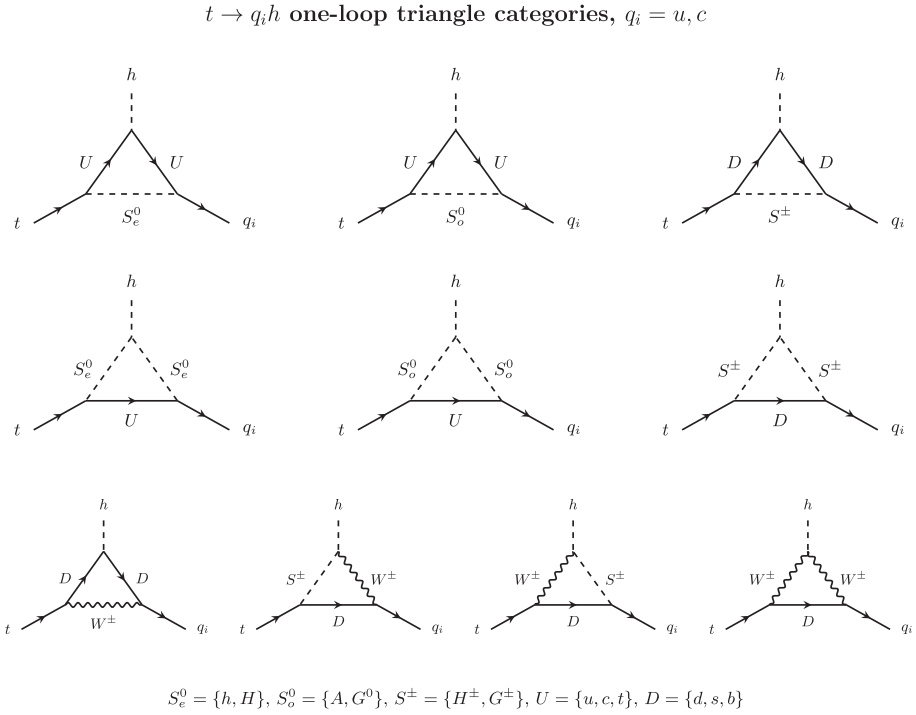


FIG. 2. One-loop triangle categories for the top-FCNC channels $t \to q_i h$ with $q_i = u$, c. The notation is the same as in Fig. 1(a).

$$\mathrm{BR}(h \to e\mu) < 4.4 \times 10^{-5}, \quad \mathrm{BR}(h \to e\tau) < 2.0 \times 10^{-3}, \quad \mathrm{BR}(h \to \mu\tau) < 1.5 \times 10^{-3}. \tag{40}$$

These entries correspond to the observed limits for $h \to e\mu$ [17], $h \to e\tau$ [16], and $h \to \mu\tau$ [15], respectively. The $\mu - e$ conversion constraints are imposed as [37–39]

$$\mathrm{CR}_{\mathrm{Al}} < 7.0 \times 10^{-13}, \quad \mathrm{CR}_{\mathrm{Ti}} < 4.3 \times 10^{-12}, \quad \mathrm{CR}_{\mathrm{Au}} < 7.0 \times 10^{-13}. \tag{41}$$

i Additional CLFV observables. Radiative and three-body charged-lepton-flavor-violation (CLFV) observables are evaluated as auxiliary predictions outside the independent sample-reducing cut-flow. In the surviving sample, these observables remain below their corresponding current experimental limits. The largest ratios of the predicted values to the corresponding experimental upper bounds are approximately 3.2×10^{-2} for $\mu \to e\gamma$ and 5.2×10^{-4} for $\tau \to 3\mu$, with smaller ratios in the other radiative and three-body CLFV channels. Top-FCNC and Higgs-FCNC quantities are evaluated for interpretation outside the selection cuts.

After all imposed selections, the final sample is fixed for the numerical analysis below.

E. Computational workflow

The model implementation and SPheno interface are generated with SARAH 4.15.4 [40]. The particle spectrum, low-energy observables, and lepton-sector HFV Higgs rates are evaluated with SPheno 4.0.6 [41,42]. In particular, the neutral-meson-mixing observables are computed using the SARAH-generated SPheno/FlavorKit routines [43]. Higgs signal-strength constraints are evaluated with the HiggsSignals functionality used in the HiggsTools 1.1.3 run [44,45]. The FCNC one-loop vertex corrections are obtained using FeynArts 3.12, FormCalc 9.10, and LoopTools 2.16 [46–48], with SARAH-matched $G^{L,R}_{H^+ud}$ conjugations.

The numerical chain proceeds as follows. Scalar-sector points satisfying the theoretical and Higgs-sector preselection requirements are first generated. The charged-fermion Yukawa textures are then reconstructed in the mass and gauge bases according to the type 1B flavor structure, with the CKM rotation assigned to the down sector. The Higgs signal-strength selection is applied next, followed by the precision, flavor, and flavor-violating observable requirements. The final branching-ratio distributions and hierarchy observables are then assembled using the conventions of Sec. III A.

IV. NUMERICAL ANALYSIS

The scan ranges and observable definitions were described in Sec. III. In this section we focus on the numerical consequences for the surviving type 1B F2HDM sample.

A. Cut-flow and final sample

Starting from 50000 generated points in the parameter region summarized in Table I, 6790 points pass the global

TABLE I. Input parameter ranges and preselection requirements for the type 1B F2HDM scan.

Parameter or requirement	Range or selection
$\tan\beta = v_2/v_1$	$1 \le \tan\beta \le 30$
m_{12}^2	$(2.5\times10^5, 1.0\times10^6)$ GeV^2
λ_1	$0 \le \lambda_1 \le 3$
λ_2	$0.06 \le \lambda_2 \le 0.13$
$\lambda_{3,4,5}$	$-5 \le \lambda_{3,4,5} \le 5$
Light-Higgs mass	124 GeV $< m_h <$ 126 GeV
Heavy-scalar masses	$m_H, m_A, m_{H^\pm} > 1$ TeV
Charged-pseudoscalar splitting	$\lvert m_A - m_{H^\pm}\rvert < 200$ GeV
Alignment proxy	$\lvert\kappa_V\rvert^2 > 0.95$
O^u_{ij}	$0.1 \le \lvert O^u_{ij}\rvert \le 10$
O^d_{ii}	$0.01 \le \lvert O^d_{ii}\rvert \le 10$
$O^d_{12,21}$, $O^d_{13,31}$	$0.01 \le \lvert O^d_{ij}\rvert \le 6$
$O^d_{23,32}$	$0.01 \le \lvert O^d_{23,32}\rvert \le 1$
O^ℓ_{ij}	$1 \le \lvert O^\ell_{ij}\rvert \le 10$
Texture-factor phases	0

HiggsSignals condition $\Delta\chi^2_{\rm HS} \le 1$. Within this subset, the meson-mixing constraints reduce the sample to 1094 points, the $B \to X_s\gamma$ selection to 552 points, and the electroweak precision selection to 542 points. The direct HFV and μ–e conversion constraints do not further reduce this sample, leaving

$$N_{\rm final} = 542. \tag{42}$$

These points form the constrained surviving sample used in the following analysis; the corresponding cut-flow is shown in Fig. 3.

One-loop rate update and branching-ratio convention. Before discussing the hierarchy and parameter dependences, we specify the rate convention used in the numerical plots. The surviving sample is defined by the cut-flow above; the one-loop vertex corrections are then evaluated on this fixed sample and are not used as additional selection cuts. For the Higgs-mediated FCNC decays and rare top decays we use the rate definition of Sec. III C, namely the tree-level contribution plus the tree-loop interference and the squared one-loop amplitude. Thus, unless explicitly stated otherwise, the quoted rates for $h \to sb$, $h \to db$, $h \to uc$, $t \to ch$, and $t \to uh$ below refer to the one-loop-updated branching ratios $\mathrm{BR}_{1\mathrm{L}}$.

For the lepton-sector HFV Higgs channels, the numerical rates are those obtained from the SPheno loop calculation in the workflow of Sec. III E. Tree-level quantities are shown separately only when the text explicitly discusses tree-level stability. With this convention, the hierarchy plots in Figs. 4–6 and the parameter-driver plots in Figs. 7–9 can be read as the corrected-rate phenomenology of the final 542-point sample. The detailed size and interpretation of the relative one-loop shifts are discussed later in Sec. IV D.

B. Branching-ratio hierarchy

The eight flavor-violating channels considered in this work display a pronounced hierarchy in the surviving sample, with the ordering quoted in the rate convention of each channel. The numerically largest rates are carried by $h \to sb$, $h \to \mu\tau$, $h \to db$, and $t \to ch$; the up-sector Higgs-FCNC mode $h \to uc$, the electron-flavor HFV Higgs modes, and $t \to uh$ are much smaller.

As shown in Fig. 4, the median rates in this convention are approximately 8.43×10^{-4} for $h \to sb$, 2.59×10^{-5} for

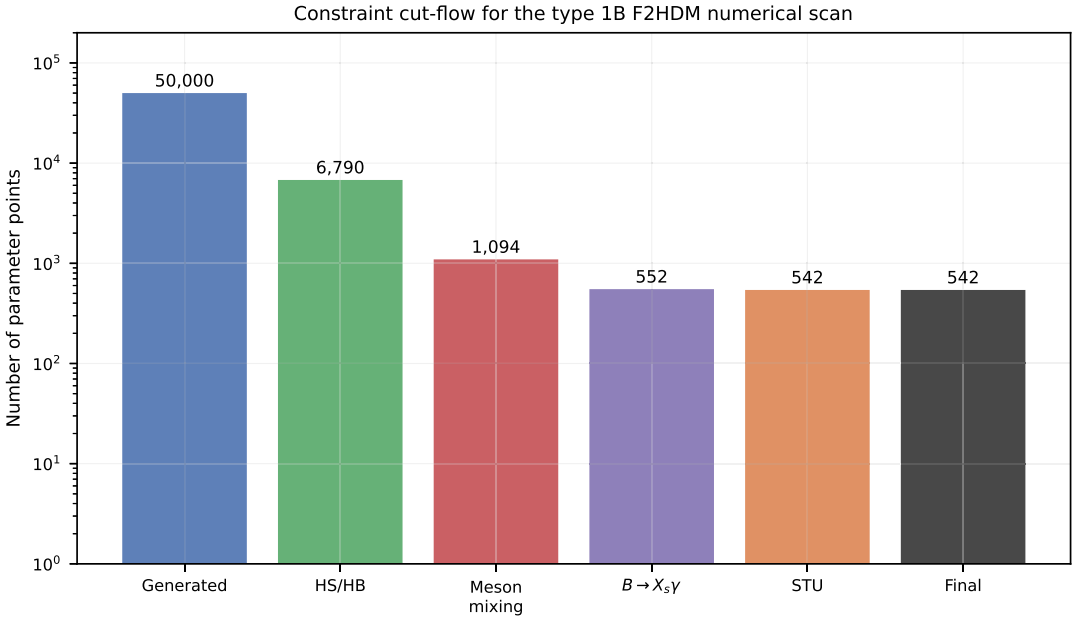


FIG. 3. Cut-flow for the type 1B F2HDM numerical scan after the Higgs, flavor, and electroweak selections.

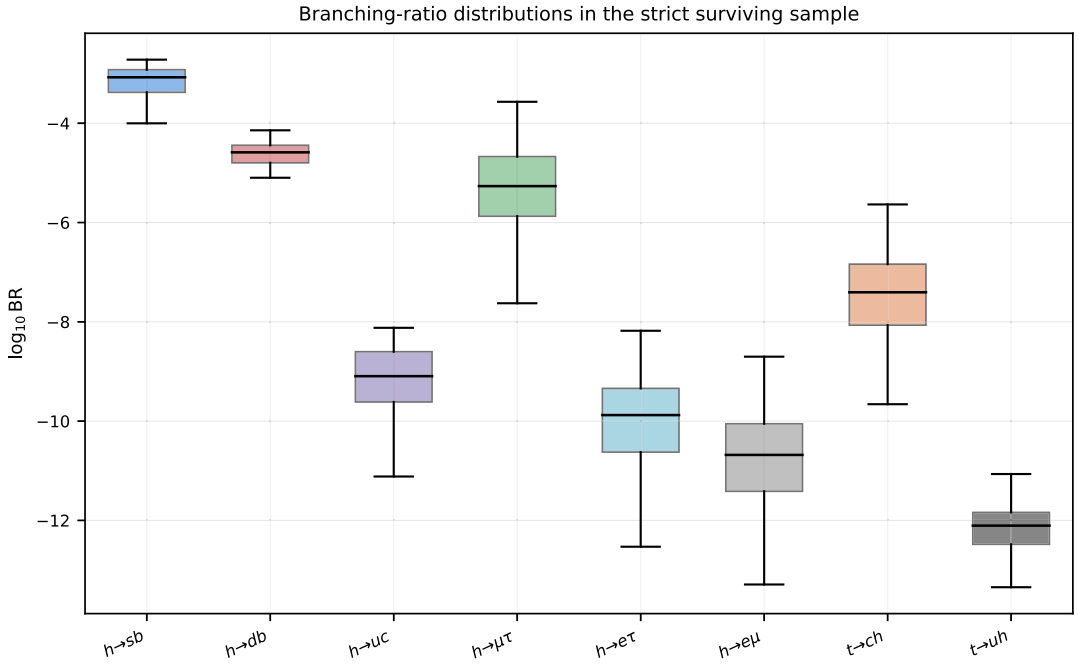


FIG. 4. Overview of the flavor-violating rates for the eight channels, shown as $\log_{10}$ BR.

$h \to db$, 8.04×10^{-10} for $h \to uc$, 5.41×10^{-6} for $h \to \mu\tau$, 3.93×10^{-8} for $t \to ch$, and 7.85×10^{-13} for $t \to uh$. The corresponding maximum branching ratios are 1.91×10^{-3} for $h \to sb$, 7.20×10^{-5} for $h \to db$, 7.57×10^{-9} for $h \to uc$, 2.70×10^{-4} for $h \to \mu\tau$, 6.68×10^{-9} for $h \to e\tau$, 2.01×10^{-9} for $h \to e\mu$, 2.32×10^{-6} for $t \to ch$, and 8.59×10^{-12} for $t \to uh$. The resulting qualitative pattern is that the two down-sector Higgs-FCNC modes satisfy

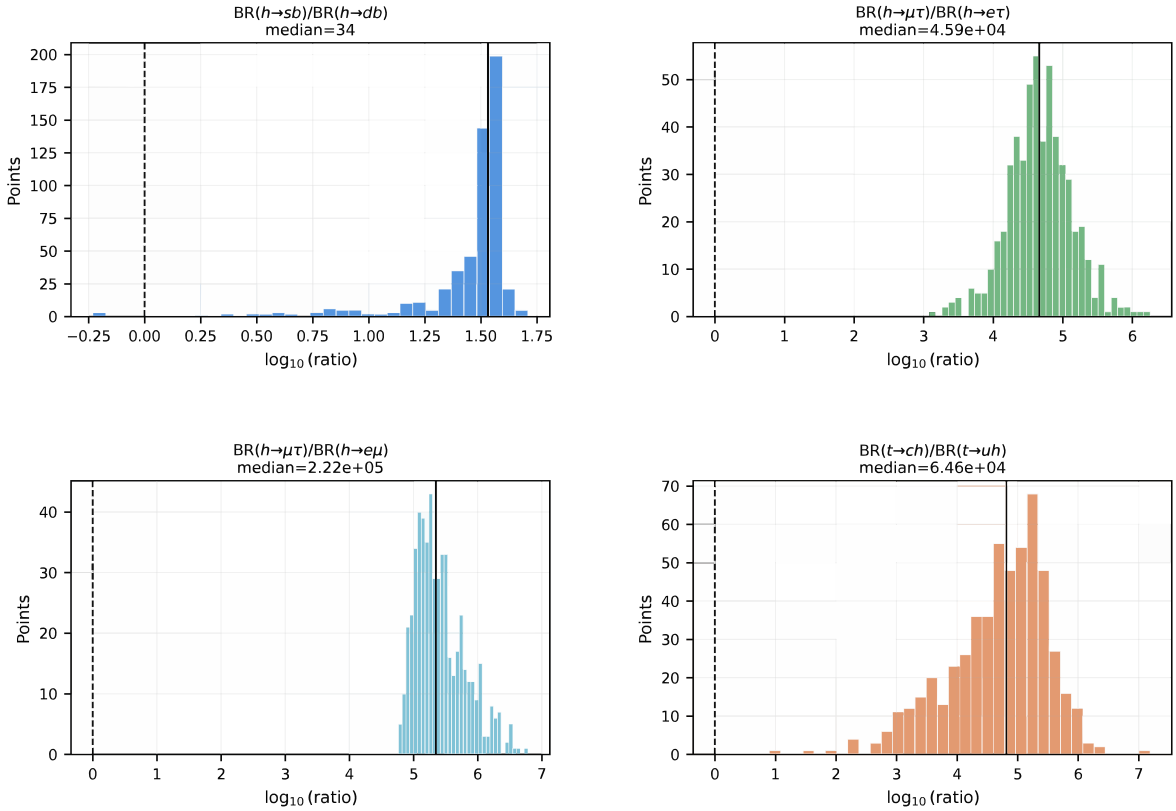


FIG. 5. Hierarchy-ratio distributions in the type 1B F2HDM sample. The dashed black vertical line marks unit ratio, i.e., $\log_{10}(\text{ratio}) = 0$, while the solid black vertical line marks the median of each distribution.

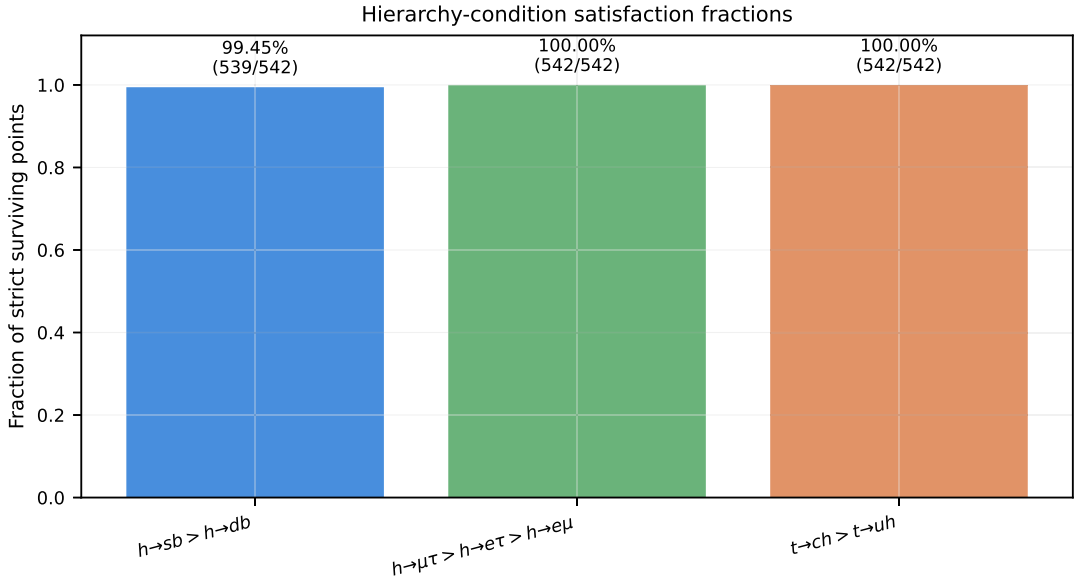


FIG. 6. Fractions of points satisfying the down sector, lepton sector, and top-sector hierarchy conditions.

$$\mathrm{BR}(h \to sb) \gg \mathrm{BR}(h \to db),$$

while the up-sector Higgs-FCNC mode $h \to uc$ is much smaller than the down-sector modes in the final sample. The lepton hierarchy is

$$\mathrm{BR}(h \to \mu\tau) \gg \mathrm{BR}(h \to e\tau), \qquad \mathrm{BR}(h \to e\mu).$$

For the top channels the ordering is $\mathrm{BR}(t \to ch) \gg \mathrm{BR}(t \to uh)$, with a median ratio $\mathrm{BR}(t \to ch)/\mathrm{BR}(t \to uh) \simeq 6.46 \times 10^4$.

The hierarchy distributions in Figs. 5 and 6 show stable down sector, lepton, and top patterns across the final sample. The median ratio $\mathrm{BR}(h \to sb)/\mathrm{BR}(h \to db)$ is about 34.0 after the one-loop rate update, and the down-sector condition holds for $539/542 = 99.45\%$ of the sample. The lepton and top-hierarchy conditions hold for all final points, with median $\mathrm{BR}(t \to ch)/\mathrm{BR}(t \to uh) \simeq 6.46 \times 10^4$. The three points with $\mathrm{BR}_{1L}(h \to db) > \mathrm{BR}_{1L}(h \to sb)$ are discussed in Sec. IV F.

C. Parameter drivers and low-energy correlations

To identify monotonic parameter dependences we use Spearman's rank coefficient,

$$\rho_S(X, Y) = \mathrm{corr}[\mathrm{rank}(X), \mathrm{rank}(Y)], \tag{43}$$

usually with $Y = \log_{10} \mathrm{BR}$. We use the alignment proxy κ_V defined in Sec. II A. We also use the effective texture combination

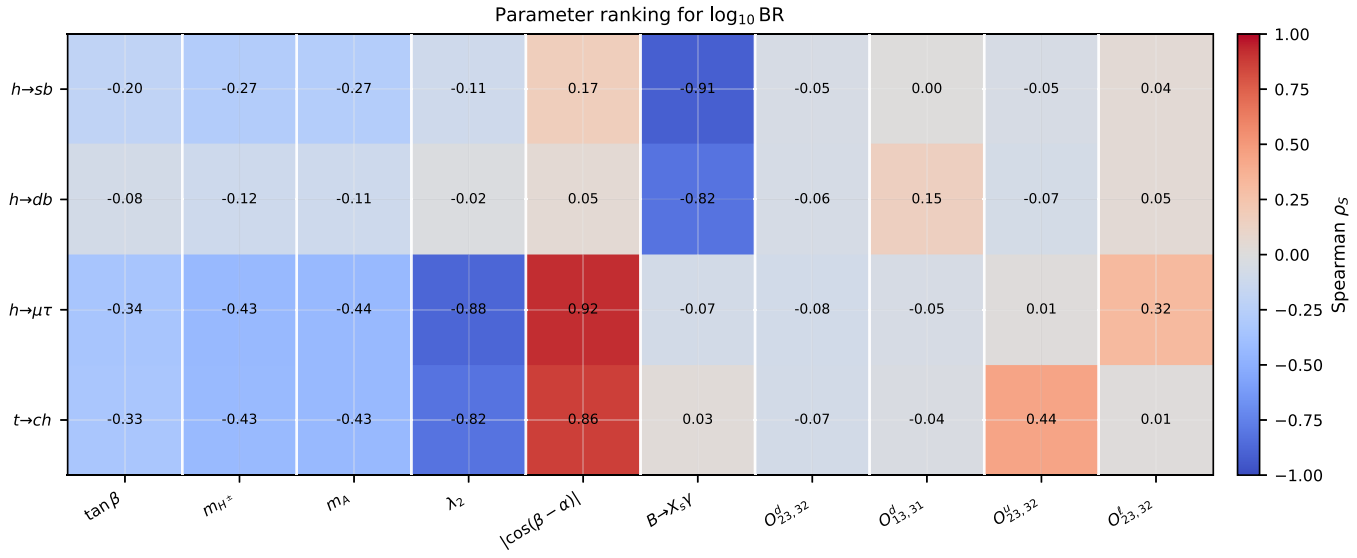


FIG. 7. Spearman-rank driver analysis for the main flavor-violating rates.

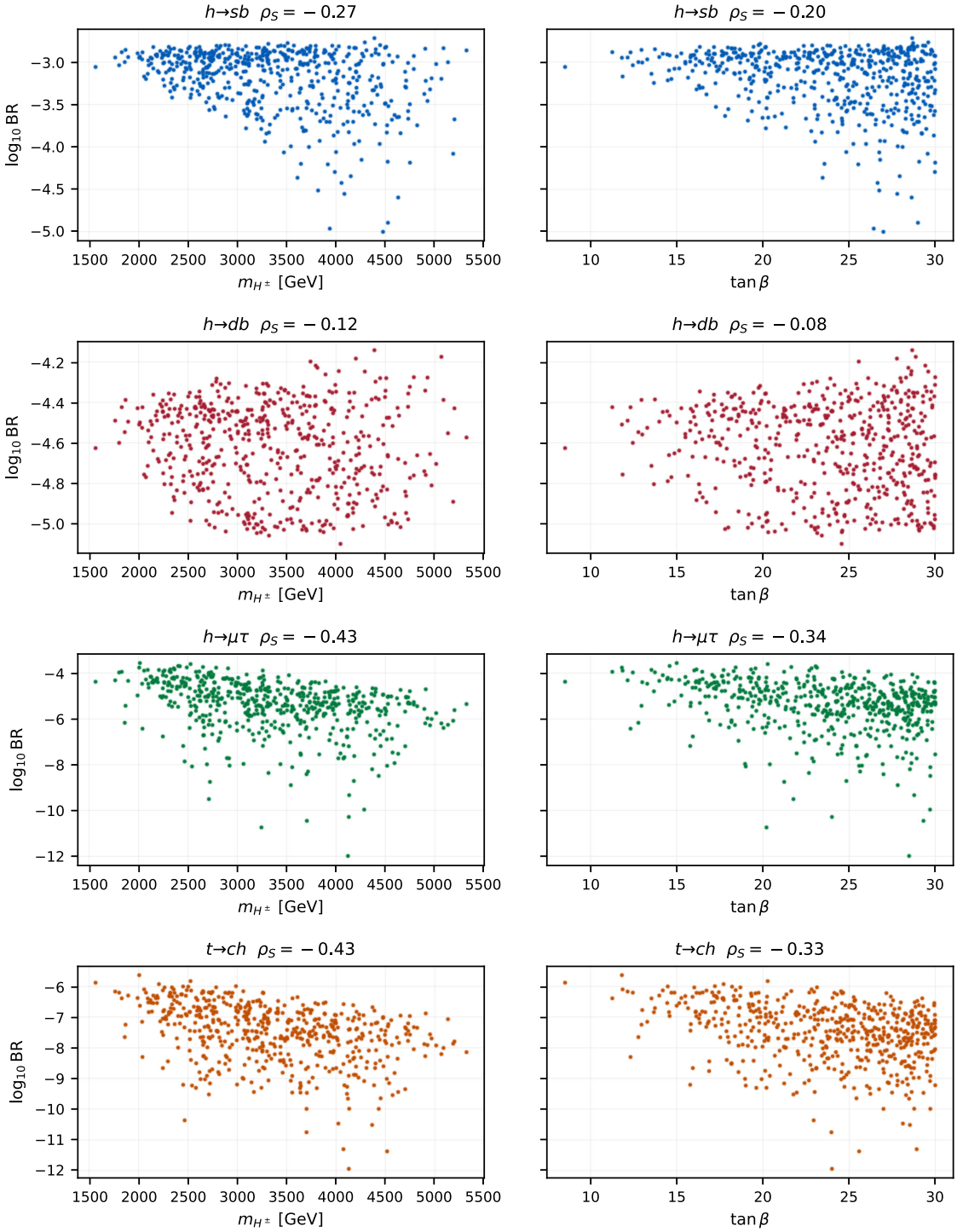


FIG. 8. Dependence of the main flavor-violating rates on $m_{H^\pm}$ and $\tan\beta$.

$$O_{\rm eff}^{f,ij} = \sqrt{\frac{|O_{ij}^f|^2 + |O_{ji}^f|^2}{2}}, \qquad f = u, d, \ell, \tag{44}$$

which is a derived quantity.

The driver ranking in Fig. 7 shows that $h \to sb$ and $h \to db$ are shaped mainly by the constrained down-sector structure and by low-energy flavor selections, with no dominant single $O(1)$ texture entry. Numerically, $\rho_S(O_{\rm eff}^{d,23}) = -0.055$ for $h \to sb$ and $\rho_S(O_{\rm eff}^{d,13}) = 0.151$ for $h \to db$, while the strongest monotonic correlation in the two down-sector rates is with $\mathrm{BR}(B \to X_s\gamma)$, $\rho_S = -0.909$, and -0.819, respectively. The $h \to \mu\tau$ rate remains strongly alignment controlled, with $\rho_S(|1 - \kappa_V|) = 0.916$, and the

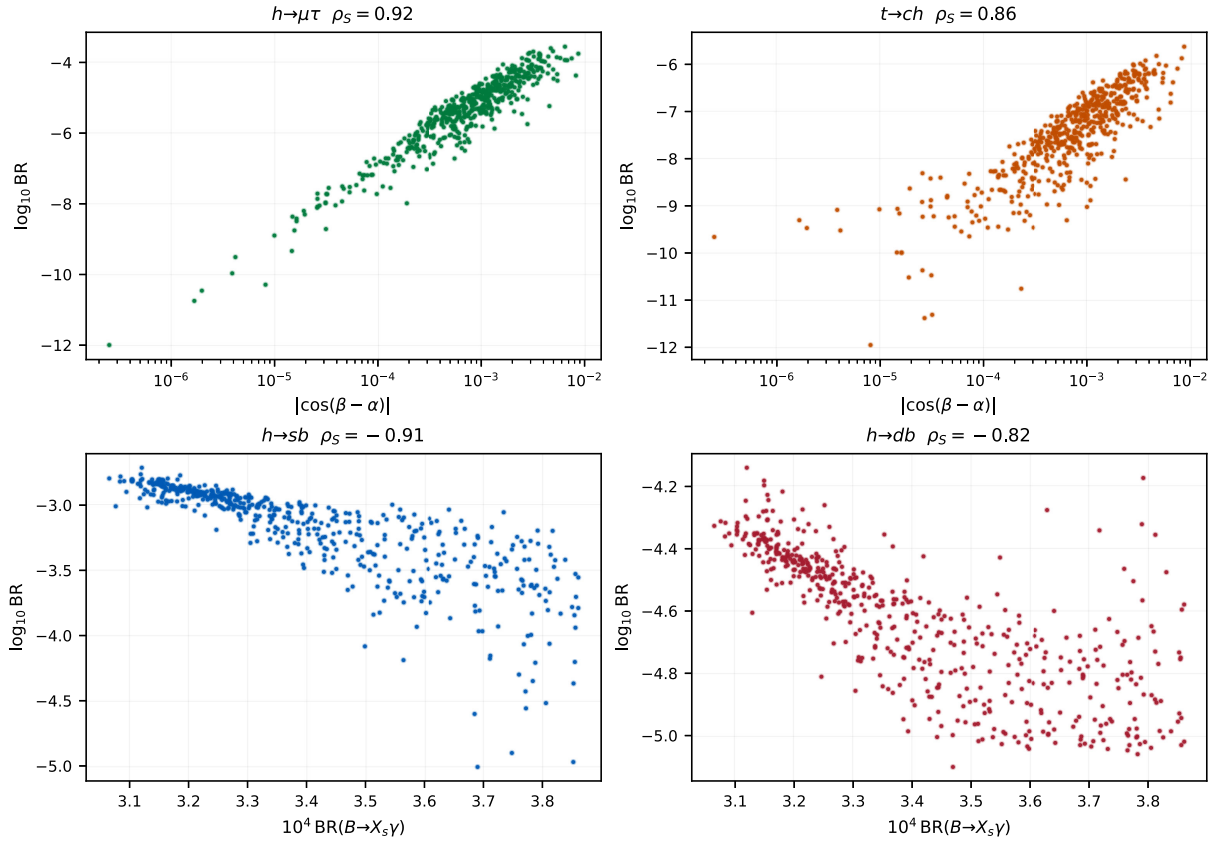


FIG. 9. Alignment and $B \to X_s\gamma$ correlations for the main flavor-violating rates.

$t \to ch$ rate also has a positive alignment correlation, $\rho_S(|1-\kappa_V|) = 0.862$.

Figure 8 shows that the down-sector Higgs-FCNC rates in the final sample retain only mild direct monotonic dependence on $m_{H^\pm}$ and $\tan\beta$ once the stronger flavor selections are imposed; for example $\rho_S(\tan\beta, \log_{10}\mathrm{BR}) = -0.200$ for $h \to sb$ and -0.075 for $h \to db$. The $h \to \mu\tau$ and $t \to ch$ rates are more visibly alignment controlled, with additional negative correlations with λ_2 in the driver ranking. The alignment panels in Fig. 9 show that $h \to \mu\tau$ remains strongly alignment controlled, while the $t \to ch$ rate has a positive alignment correlation and a compressed absolute range. The same figure also shows the strong $B \to X_s\gamma$ correlation in the down-sector channels.

TABLE II. One-loop relative-correction quantiles for the quark and top-FCNC channels in the strict surviving sample.

Channel	Min	5%	Median	95%	Max
$t \to ch$	−0.956	−0.248	−0.0927	3.07	3.06×10^4
$t \to uh$	−0.91	−0.0931	1.11	485	2.74×10^7
$h \to uc$	−0.716	49.7	4.09×10^3	2.14×10^6	4.25×10^{10}
$h \to sb$	−0.993	−0.906	−0.444	−0.0473	0.252
$h \to db$	−0.828	−0.78	−0.422	0.0485	0.624

D. One-loop vertex effects

Having fixed the corrected-rate convention above, we now quantify the size of the vertex effects in Higgs-mediated FCNC decays and rare top decays. The relative quantities in Table II are computed with the triangle categories shown in Figs. 1(a) and 2.

For $t \to ch$, very large positive relative corrections occur in the one-loop rate comparison. These large ratios are primarily denominator effects caused by very small tree-level rates near the alignment region; the corresponding absolute physical branching ratios remain small. For this channel the relative correction can be written as

$$\delta_{1\mathrm{L}} = \frac{|\mathcal{M}_{\mathrm{tree}} + \mathcal{M}_{\mathrm{loop}}|^2 - |\mathcal{M}_{\mathrm{tree}}|^2}{|\mathcal{M}_{\mathrm{tree}}|^2} = 2\mathrm{Re}\left(\frac{\mathcal{M}_{\mathrm{loop}}}{\mathcal{M}_{\mathrm{tree}}}\right) + \left|\frac{\mathcal{M}_{\mathrm{loop}}}{\mathcal{M}_{\mathrm{tree}}}\right|^2.$$

Near the alignment region, the tree-level tch coupling is strongly suppressed, so $\mathrm{BR}_{\mathrm{tree}}(t \to ch)$ becomes very small.

Figure 10 illustrates this denominator effect in more detail. In panel (a), the largest values of $\delta_{1\mathrm{L}}$ appear close to the alignment region. Panel (b) shows that the same region contains very small tree-level $t \to ch$ branching ratios.

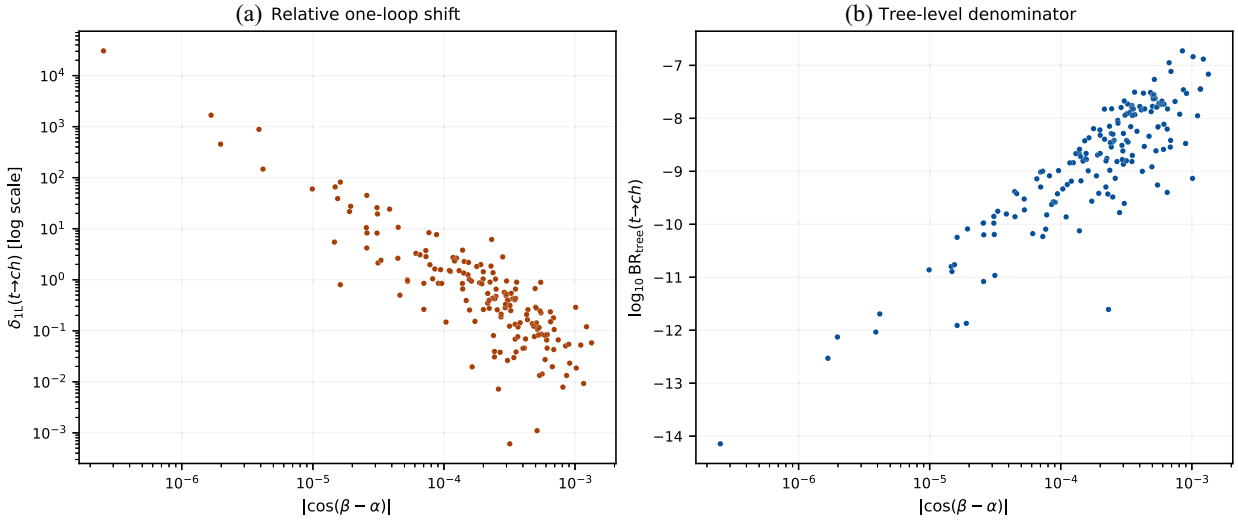


FIG. 10. Alignment dependence in the $t \to ch$ channel: (a) δ_{1L} on a logarithmic scale and (b) $\log_{10} \mathrm{BR}_{\mathrm{tree}}$ as functions of $|\cos(\beta-\alpha)|$.

The corresponding one-loop-updated branching ratio is shown in Fig. 9(b), where the absolute $t \to ch$ rate remains small and compressed. The large values of δ_{1L} should therefore be interpreted as relative ratios in tree-suppressed regions, not as evidence for a parametrically large absolute one-loop-induced $t \to ch$ branching ratio. For $h \to sb$ and $h \to db$, the median one-loop relative corrections are negative, $\delta_{1L} \simeq -0.444$ and -0.422, respectively, indicating a net suppression in the down-sector channels.

E. Tree-level stability and CKM-down origin

A striking feature of the surviving sample is the different width of the tree-level branching-ratio distributions. The tree-level quantiles in Table III show that $h \to sb$ and $h \to db$ are locked into narrow bands, while representative up-sector Higgs and top-FCNC rates span several orders of magnitude.

The down-sector central 5–95% intervals are $[1.46, 1.57] \times 10^{-3}$ for $h \to sb$ and $[4.14, 4.64] \times 10^{-5}$ for $h \to db$. In contrast, the corresponding intervals are 1.08×10^{-10} to 7.17×10^{-7} for $t \to ch$ and 3.51×10^{-16} to 5.35×10^{-12} for $h \to uc$.

The stability can be traced directly to the mass-basis reconstruction in Sec. II B. In the down-sector matrix of Eq. (15), the entries relevant for $h \to sb$ contain

$$(M'_d)_{23} = -V^*_{ts} m_b \left(1 + O^d_{23} \frac{m_s}{m_b}\right), \qquad (M'_d)_{32} = O^d_{32} m_s. \tag{45}$$

The dependence on O^d_{23} is suppressed by m_s/m_b, so the leading structure is the fixed CKM-weighted term $-V^*_{ts} m_b$; the opposite-chirality-related entry is only m_s-sized. Similarly, for $h \to db$,

$$(M'_d)_{13} = -V^*_{td} m_b \left(1 + O^d_{13} \frac{m_s}{m_b}\right), \qquad (M'_d)_{31} = O^d_{31} m_d. \tag{46}$$

The leading fixed term $-V^*_{td} m_b$ dominates over the scanned O^d-dependent pieces. This explains why the down-sector tree-level branching ratios are only weakly sensitive to the scanned O^d factors and form narrow bands. Their remaining variation is tied to the fixed CKM factors, mass reconstruction, Higgs mixing/alignment, and the surviving flavor and electroweak constraints.

This behavior contrasts with $t \to ch$, $h \to uc$, and the lepton-sector $h \to \mu\tau$ rate. In Eq. (14), the relevant up-sector off-diagonal entries are controlled by the scanned O^u texture factors and by alignment-dependent Higgs mixing; the fixed CKM-weighted m_b leading term is a special

TABLE III. Tree-level branching-ratio quantiles for the main channels in the strict surviving sample.

Channel	Minimum	5th percentile	Median	95th percentile	Maximum
$h \to sb$	1.37×10^{-3}	1.46×10^{-3}	1.54×10^{-3}	1.57×10^{-3}	1.57×10^{-3}
$h \to db$	3.81×10^{-5}	4.14×10^{-5}	4.49×10^{-5}	4.64×10^{-5}	4.66×10^{-5}
$t \to ch$	7.17×10^{-15}	1.08×10^{-10}	4.65×10^{-8}	7.17×10^{-7}	2.71×10^{-6}
$h \to \mu\tau$	1.04×10^{-12}	1.91×10^{-8}	5.27×10^{-6}	8.26×10^{-5}	2.65×10^{-4}

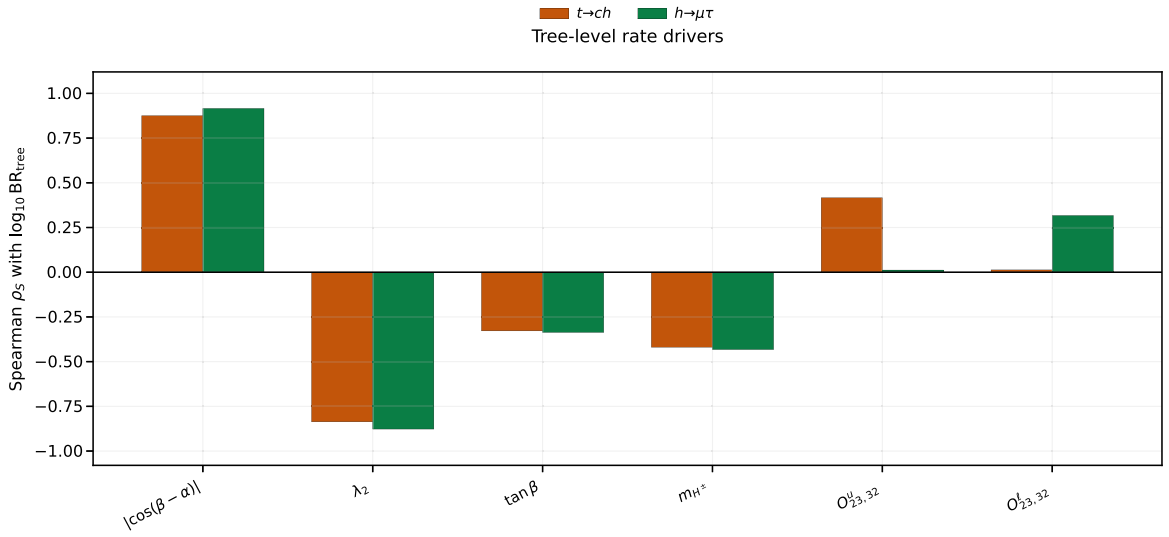


FIG. 11. Spearman correlations for representative tree-level Higgs and top-FCNC branching ratios in the final sample.

feature of the down-sector entries. In Eq. (16), the relevant lepton-sector entries are controlled by $O^{\ell}_{23}m_{\mu}$ and $O^{\ell}_{32}m_{\mu}$. Consequently, the non-down-sector flavor-violating rates remain more sensitive to scanned texture entries, alignment, and accidental cancellations among Higgs-doublet contributions.

The broad non-down-sector distributions are visible in the driver plot of Fig. 11 and the λ_2-alignment scatter plot of Fig. 12. These channels reflect their direct sensitivity to the scanned up- and lepton-sector textures, the alignment limit, and accidental cancellations among Higgs-doublet contributions.

F. Rare hierarchy inversion in $h \to db$ versus $h \to sb$

A small group of three points satisfies $\mathrm{BR}_{\mathrm{1L}}(h \to db) > \mathrm{BR}_{\mathrm{1L}}(h \to sb)$ after the one-loop rate is applied. All three inversion points retain the tree-level ordering $\mathrm{BR}_{\mathrm{tree}}(h \to sb) > \mathrm{BR}_{\mathrm{tree}}(h \to db)$, as summarized in Table IV. We define

$$K_{sb} = \frac{\mathrm{BR}_{\mathrm{1L}}(h \to sb)}{\mathrm{BR}_{\mathrm{tree}}(h \to sb)}, \quad K_{db} = \frac{\mathrm{BR}_{\mathrm{1L}}(h \to db)}{\mathrm{BR}_{\mathrm{tree}}(h \to db)}. \tag{47}$$

The inversion appears as a correction-factor inversion and is traced to destructive tree-loop interference in the down-sector channels. In the final sample, the inverted points have $K_{sb} \simeq (6.5 - 8.2) \times 10^{-3}$ and $K_{db} \simeq 0.34 - 0.47$, with median values $K_{sb} = 7.1 \times 10^{-3}$ and $K_{db} = 0.41$. Thus K_{db}/K_{sb} is large enough to overcome the underlying tree-level hierarchy even though the tree-level branching ratios keep $h \to sb$ above $h \to db$. Schematically,

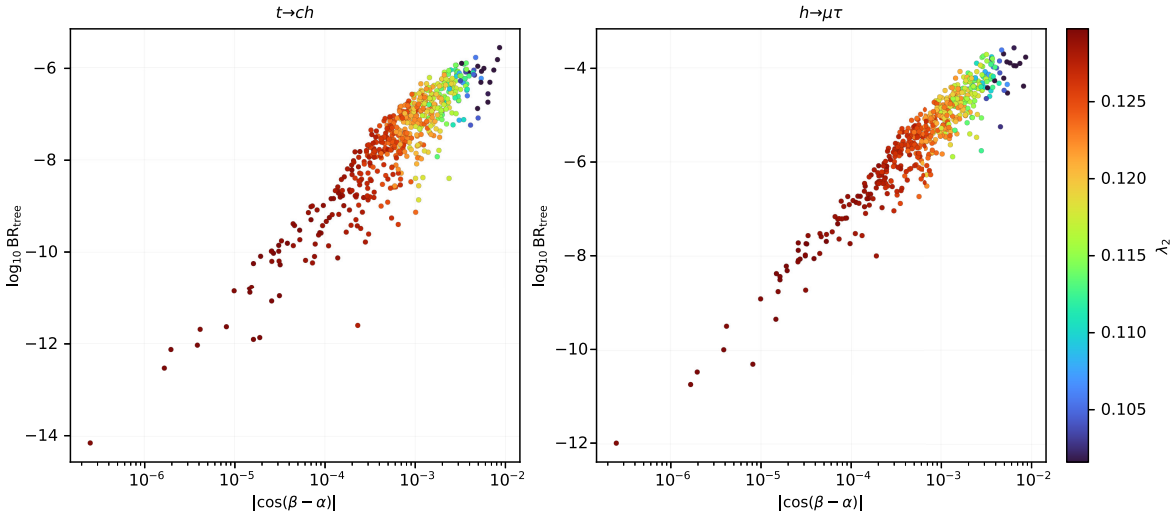


FIG. 12. Correlation of λ_2 and the alignment proxy with the loop-level $h \to \mu\tau$ rate and representative tree-level FCNC rates.

TABLE IV. Summary of the rare $h \to db > h \to sb$ hierarchy-inversion points after applying one-loop rates in the strict surviving sample.

Quantity	Inversion points
Number of inversion points	3
Inversion fraction	0.55%
Median tree ratio $\mathrm{BR}_{\mathrm{tree}}(h \to sb)/\mathrm{BR}_{\mathrm{tree}}(h \to db)$	34.2
Median one-loop ratio $\mathrm{BR}_{\mathrm{1L}}(h \to sb)/\mathrm{BR}_{\mathrm{1L}}(h \to db)$	0.592
Median $K_{sb} = \mathrm{BR}_{\mathrm{1L}}(h \to sb)/\mathrm{BR}_{\mathrm{tree}}(h \to sb)$	7.08×10^{-3}
Median $K_{db} = \mathrm{BR}_{\mathrm{1L}}(h \to db)/\mathrm{BR}_{\mathrm{tree}}(h \to db)$	0.412
Median K_{db}/K_{sb}	57.5
All inversion points keep tree-level $h \to sb > h \to db$	yes

$$K_q = \frac{|\mathcal{M}^q_{\mathrm{tree}} + \mathcal{M}^q_{\mathrm{loop}}|^2}{|\mathcal{M}^q_{\mathrm{tree}}|^2} = 1 + \delta^q_{\mathrm{int}} + R^q_{\mathrm{loop}}, \quad q = sb, db, \tag{48}$$

with

$$\delta^q_{\mathrm{int}} = \frac{2\mathrm{Re}[(\mathcal{M}^q_{\mathrm{tree}})^* \mathcal{M}^q_{\mathrm{loop}}]}{|\mathcal{M}^q_{\mathrm{tree}}|^2},$$
$$R^q_{\mathrm{loop}} = \frac{|\mathcal{M}^q_{\mathrm{loop}}|^2}{|\mathcal{M}^q_{\mathrm{tree}}|^2},$$
$$C^q_{\mathrm{int}} \equiv \frac{\mathrm{Re}[(\mathcal{M}^q_{\mathrm{tree}})^* \mathcal{M}^q_{\mathrm{loop}}]}{|\mathcal{M}^q_{\mathrm{tree}}||\mathcal{M}^q_{\mathrm{loop}}|}, \quad q = sb, db. \tag{49}$$

The small K_{sb} values therefore indicate a near cancellation in the total $h \to sb$ amplitude, while the corresponding $h \to db$ rates are suppressed less severely.

Figure 13 shows that the three inverted points lie in the region with strongly negative C^{sb}_{int}, while C^{db}_{int} is less extreme. The enlarge panel resolves the three surviving inverted points individually. The presence of these three inversion points shows that the destructive-interference mechanism survives the stringent meson-mixing constraints.

G. Lepton-sector HFV tree-level and one-loop comparison

In the final sample, Fig. 14 compares the tree-level and SPheno one-loop branching ratios for the three lepton-sector HFV Higgs channels. The points lie close to the equal-rate line, showing that the one-loop corrections are generally small over the surviving parameter space.

H. Experimental prospects and interpretation

The hierarchy found in Sec. IV B is a model hierarchy in the surviving type 1B parameter sample; LHC observability requires separate detector-level information. The channel $h \to sb$ can reach the 10^{-3} level in branching ratio, but its experimental reconstruction is challenging because the final state is embedded in ordinary hadronic Higgs decays and requires flavor-sensitive strange- and bottom-jet information. A direct collider interpretation would therefore need a dedicated analysis with realistic b-tagging, possible

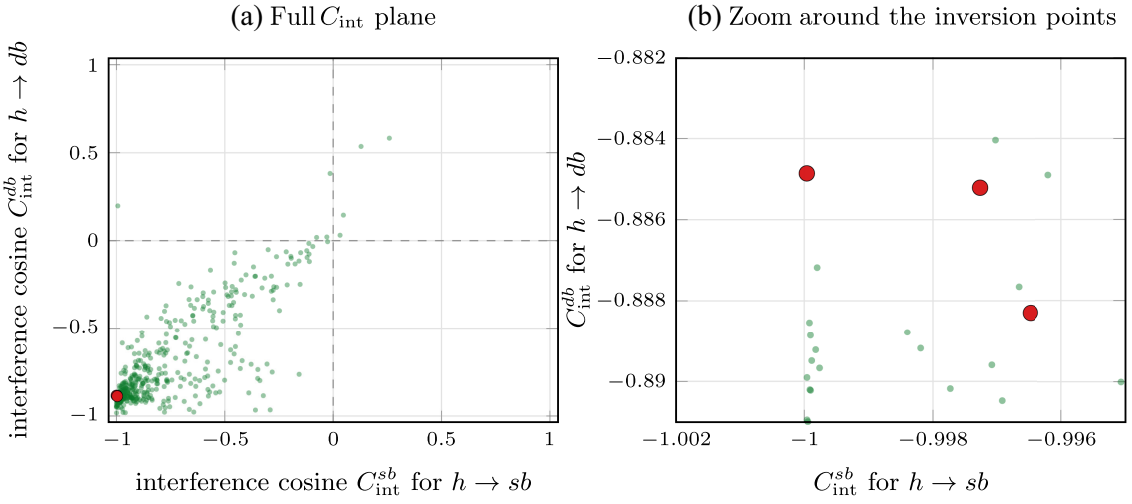


FIG. 13. Interference-cosine projection of the rare hierarchy inversion. Panel (a) shows the full C^{sb}_{int}-C^{db}_{int} plane, and panel (b) enlarges into the inversion region. Green points show noninverted points, while red points show the three points with $\mathrm{BR}_{\mathrm{1L}}(h \to db) > \mathrm{BR}_{\mathrm{1L}}(h \to sb)$, after summing the charge-conjugate final states.

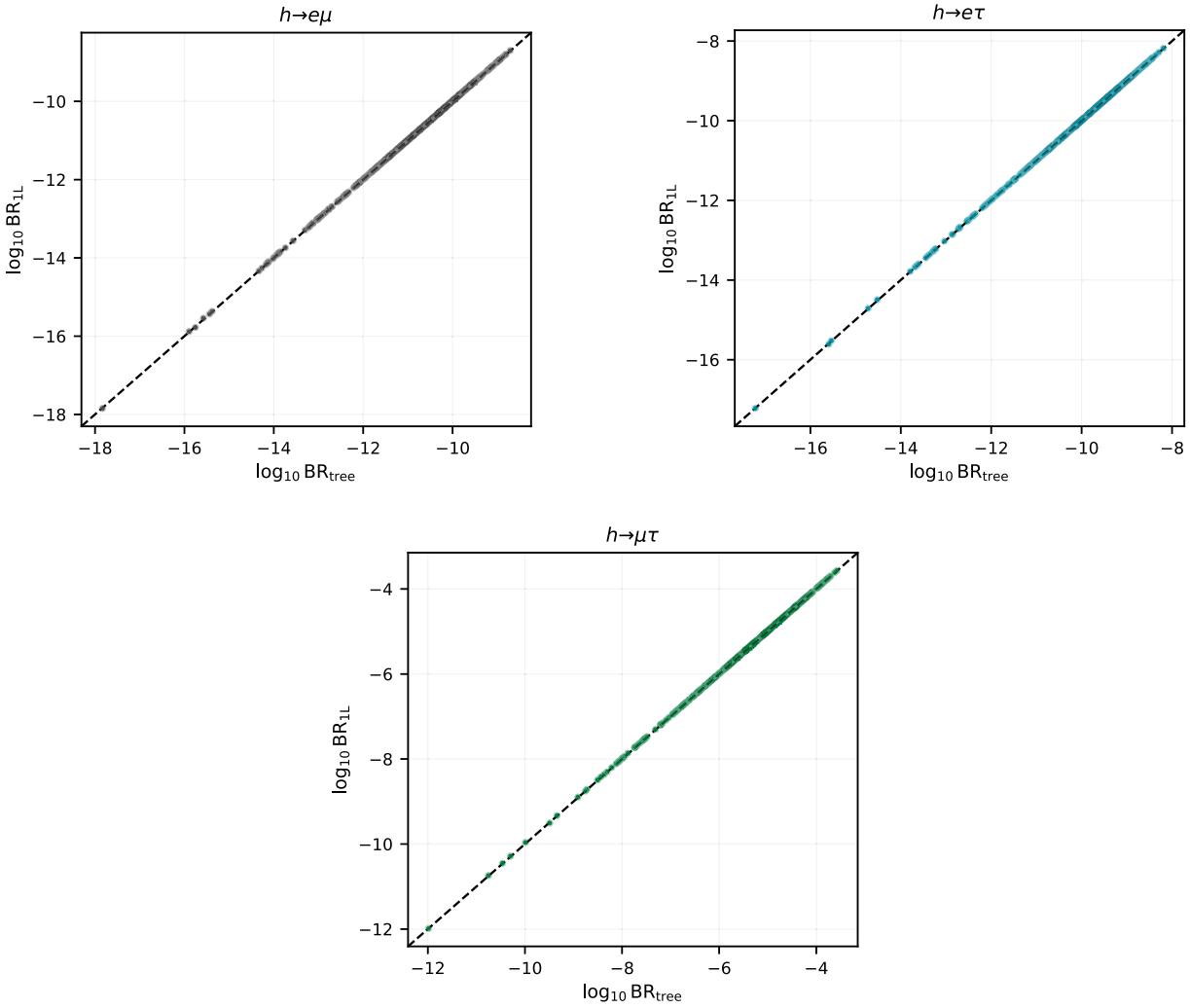


FIG. 14. Comparison of the tree-level and SPheno one-loop branching ratios for the lepton-sector HFV channels in the 542-point final sample. The dashed diagonal line in each panel denotes $\mathrm{BR}_{1L} = \mathrm{BR}_{\mathrm{tree}}$.

strange-tagging, or strange-enriched categories, and detector-level efficiencies.

The lepton-sector HFV mode $h \to \mu\tau$ is experimentally cleaner. The limits in Table V show 10^{-3}-level sensitivity in $h \to e\tau$ and $h \to \mu\tau$, and a stronger 10^{-5}-level bound in $h \to e\mu$. The values obtained in the surviving sample are below current bounds but can lie in a range relevant for improved Run-3 and high-luminosity LHC analyses. By contrast, $h \to e\tau$ and $h \to e\mu$ are typically much smaller in this type 1B realization.

For top-Higgs FCNCs, current direct limits reach the 10^{-4} level. Both the tree-level texture hierarchy and the loop-corrected rates emphasize $t \to ch$ over $t \to uh$ in the surviving sample. Future reinterpretations should combine the model-specific flavor structure with realistic top reconstruction, Higgs decay modes, flavor tagging, and

TABLE V. Current direct experimental upper limits or direct-limit status for the flavor-violating channels considered in this work.

Channel	Direct bound/status	Source
$h \to e\mu$	$\mathrm{BR} < 4.4 \times 10^{-5}$ at 95% C.L.	CMS [17]
$h \to e\tau$	$\mathrm{BR} < 2.0 \times 10^{-3}$ at 95% C.L.	ATLAS [16]
$h \to \mu\tau$	$\mathrm{BR} < 1.5 \times 10^{-3}$ at 95% C.L.	CMS [15]
$t \to uh$	$\mathrm{BR} < 2.6 \times 10^{-4}$ at 95% C.L.	ATLAS [24]
$t \to ch$	$\mathrm{BR} < 3.4 \times 10^{-4}$ at 95% C.L.	ATLAS [24]
$h \to sb, h \to db, h \to uc$	No dedicated process-specific direct upper limit is currently available; present constraints on quark-flavor Higgs couplings are indirect or analysis dependent.	[26,29]

correlations with the low-energy constraints. Thus the most promising phenomenological targets depend on both rate size and experimental accessibility: $h \to sb$ is numerically large but experimentally difficult, $h \to \mu\tau$ is cleaner, and $t \to ch$ provides the leading top-flavor probe in this numerical analysis.

V. CONCLUSIONS

We have studied flavor-violating Higgs and top decays in the type 1B flavorful two-Higgs-doublet model with a twist. Generation-dependent doublet assignments make the Yukawa sector neither natural-flavor-conserving nor aligned, so tree-level scalar FCNCs arise. They are organized by the approximate $U(2)^5$ texture and, in our implementation, by a CKM matrix generated in the down sector. Unlike a generic 2HDM with tree-level FCNCs, where off-diagonal Yukawa couplings are often treated as more freely parametrized, type 1B ties them to these assignments and the CKM-down mass reconstruction, yielding correlated flavor hierarchies.

After imposing Higgs, electroweak, meson-mixing, $B \to X_s\gamma$, HFV, and CLFV constraints (including μ–e conversion), the surviving sample exhibits $\mathrm{BR}(h \to sb) \gg \mathrm{BR}(h \to db)$, $\mathrm{BR}(h \to \mu\tau) \gg \mathrm{BR}(h \to e\tau), \mathrm{BR}(h \to e\mu)$, and $\mathrm{BR}(t \to ch) \gg \mathrm{BR}(t \to uh)$. The leading channels are $h \to sb$, $t \to ch$, $h \to db$, and $h \to \mu\tau$. The tree-level rates for $h \to sb$ and $h \to db$ are narrowly distributed and CKM-controlled by the fixed $-V_{ts}^* m_b$ and $-V_{td}^* m_b$ terms, whereas $t \to ch$ and $h \to \mu\tau$ vary by orders of magnitude because of texture and alignment sensitivity. Approximate first-second-generation protection suppresses $h \to uc$ and $h \to e\mu$. Radiative and three-body CLFV observables remain below current limits and are not used as additional sample-reducing cuts.

We also included one-loop vertex effects, including the loop-amplitude-squared contribution to the rates. Large relative corrections in $t \to ch$ occur when alignment suppresses the tree-level coupling, although the absolute branching ratio remains small. Rare points with $\mathrm{BR}_{1\mathrm{L}}(h \to db) > \mathrm{BR}_{1\mathrm{L}}(h \to sb)$ arise from strong destructive tree-loop interference that suppresses $h \to sb$ more strongly than $h \to db$. The overall pattern nevertheless remains $h \to sb$ as the largest quark-HFV mode, $h \to \mu\tau$ as the cleanest lepton-HFV mode, and $t \to ch$ as the leading top-flavor probe.

ACKNOWLEDGMENTS

This work was supported by the National Natural Science Foundation of China (NNSFC) under Grants No. 12075074, No. 12235008, No. 11535002, and No. 11705045; the Natural Science Foundation for Distinguished Young Scholars of Hebei Province under Grant No. A2022201017; the Youth Top-notch Talent Support Program of Hebei Province; and the Midwest Universities Comprehensive Strength Promotion Project.

DATA AVAILABILITY

There are no publicly available research data or software supporting this manuscript. Requests for further information or data should be sent to the authors.

APPENDIX: REPRESENTATIVE K^0-$\bar{K}^0$ MIXING CONTRIBUTIONS

The meson-mixing observables are evaluated using the SARAH-generated SPheno/FlavorKit routines [43]. Representative contributions to K^0-$\bar{K}^0$ mixing are shown in Fig. 15.

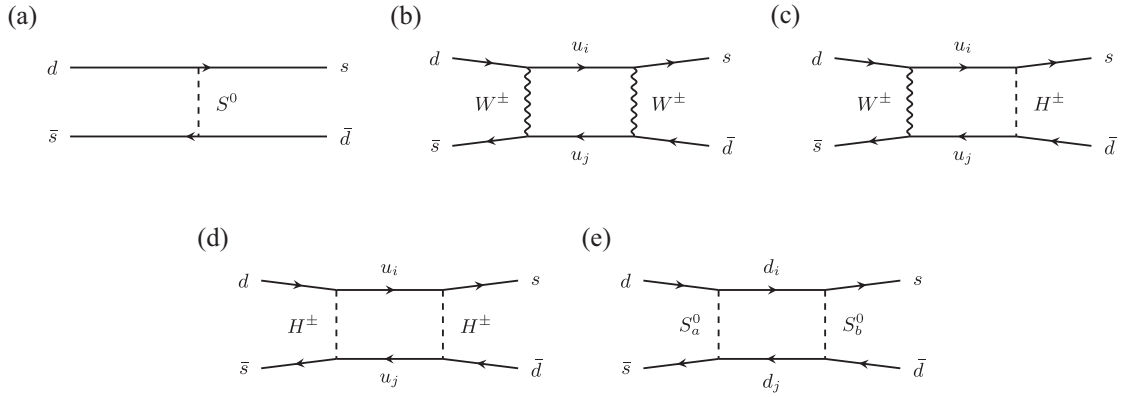


FIG. 15. Representative contributions to K^0-$\bar{K}^0$ mixing entering the SPheno/FlavorKit evaluation: (a) tree-level neutral-scalar exchange, (b) SM reference $W^\pm$–$W^\pm$ box, (c) mixed $W^\pm$–$H^\pm$ boxes, (d) $H^\pm$–$H^\pm$ boxes, and (e) neutral-scalar boxes. The mixed $W^\pm$–$H^\pm$ panel represents both boson orderings, and sums over internal flavors are implicit. Additional Goldstone-boson and neutral-gauge contributions present in the generated Wilson coefficients are not displayed separately. The diagrams are representative rather than an exhaustive graphical enumeration.

[1] ATLAS Collaboration, Phys. Lett. B **716**, 1 (2012).
[2] CMS Collaboration, Phys. Lett. B **716**, 30 (2012).
[3] S. L. Glashow and S. Weinberg, Phys. Rev. D **15**, 1958 (1977).
[4] E. A. Paschos, Phys. Rev. D **15**, 1966 (1977).
[5] A. Pich and P. Tuzon, Phys. Rev. D **80**, 091702 (2009).
[6] G. C. Branco, P. M. Ferreira, L. Lavoura, M. N. Rebelo, M. Sher, and J. P. Silva, Phys. Rep. **516**, 1 (2012).
[7] T. P. Cheng and M. Sher, Phys. Rev. D **35**, 3484 (1987).
[8] D. Atwood, L. Reina, and A. Soni, Phys. Rev. D **55**, 3156 (1997).
[9] W.-S. Hou, Phys. Lett. B **296**, 179 (1992).
[10] G. C. Branco, W. Grimus, and L. Lavoura, Phys. Lett. B **380**, 119 (1996).
[11] F. J. Botella, G. C. Branco, A. Carmona, M. Nebot, L. Pedro, and M. N. Rebelo, J. High Energy Phys. 07 (2014) 078.
[12] F. J. Botella, G. C. Branco, M. Nebot, and M. N. Rebelo, Eur. Phys. J. C **76**, 161 (2016).
[13] W. Altmannshofer, S. Gori, D. J. Robinson, and D. Tuckler, J. High Energy Phys. 03 (2017) 129.
[14] W. Altmannshofer and B. Maddock, Phys. Rev. D **98**, 075005 (2018).
[15] CMS Collaboration, Phys. Rev. D **104**, 032013 (2021).
[16] ATLAS Collaboration, J. High Energy Phys. 07 (2023) 166.
[17] CMS Collaboration, Phys. Rev. D **108**, 072004 (2023).
[18] W. Altmannshofer, C. Caillol, M. Dam, S. Xella, and Y. Zhang, arXiv:2205.10576.
[19] J. A. Aguilar-Saavedra, Acta Phys. Pol. B **35**, 2695 (2004).
[20] Z.-f. Ge and J.-l. Yang, Eur. Phys. J. C **84**, 1189 (2024).
[21] J.-L. Yang, T.-F. Feng, H.-B. Zhang, G.-Z. Ning, and X.-Y. Yang, Eur. Phys. J. C **78**, 438 (2018).
[22] CMS Collaboration, J. High Energy Phys. 02 (2022) 169.
[23] ATLAS Collaboration, J. High Energy Phys. 12 (2023) 195.
[24] ATLAS Collaboration, Eur. Phys. J. C **84**, 757 (2024).
[25] G. Blankenburg, J. Ellis, and G. Isidori, Phys. Lett. B **712**, 386 (2012).
[26] R. Harnik, J. Kopp, and J. Zupan, J. High Energy Phys. 03 (2012) 026.
[27] J. Kopp and M. Nardecchia, J. High Energy Phys. 10 (2014) 156.
[28] M. Buschmann, J. Kopp, J. Liu, and X.-P. Wang, J. High Energy Phys. 06 (2016) 149.
[29] J. Herrero-Garcia, M. Nebot, F. Rajec, M. White, and A. G. Williams, J. High Energy Phys. 02 (2019) 147.
[30] G. Abbas, A. Celis, X.-Q. Li, J. Lu, and A. Pich, J. High Energy Phys. 06 (2015) 005.
[31] W. Altmannshofer, J. Eby, S. Gori, M. Lotito, M. Martone, and D. Tuckler, Phys. Rev. D **94**, 115032 (2016).
[32] W. Altmannshofer, B. Maddock, and D. Tuckler, Phys. Rev. D **100**, 015003 (2019).
[33] Z. Cao, J.-L. Yang, T.-B. Hou, and T.-F. Feng, Phys. Rev. D **113**, 016012 (2026).
[34] S. Navas *et al.* (Particle Data Group), Phys. Rev. D **110**, 030001 (2024).
[35] M. Bona *et al.* (UTfit Collaboration), J. High Energy Phys. 03 (2008) 049.
[36] Y. Amhis *et al.* (HFLAV Collaboration), Eur. Phys. J. C **77**, 895 (2017).
[37] L. Bartoszek *et al.* (Mu2e Collaboration), Fermilab Technical Report, 2014, 10.2172/1172555.
[38] C. Dohmen *et al.* (SINDRUM II Collaboration), Phys. Lett. B **317**, 631 (1993).
[39] W. H. Bertl *et al.* (SINDRUM II Collaboration), Eur. Phys. J. C **47**, 337 (2006).
[40] F. Staub, Comput. Phys. Commun. **185**, 1773 (2014).
[41] W. Porod, Comput. Phys. Commun. **153**, 275 (2003).
[42] W. Porod and F. Staub, Comput. Phys. Commun. **183**, 2458 (2012).
[43] W. Porod, F. Staub, and A. Vicente, Eur. Phys. J. C **74**, 2992 (2014).
[44] P. Bechtle, S. Heinemeyer, O. Stal, T. Stefaniak, and G. Weiglein, Eur. Phys. J. C **74**, 2711 (2014).
[45] P. Bechtle, D. Dercks, S. Heinemeyer, T. Klingl, T. Stefaniak, G. Weiglein, and J. Wittbrodt, Eur. Phys. J. C **81**, 145 (2021).
[46] T. Hahn, Comput. Phys. Commun. **140**, 418 (2001).
[47] T. Hahn and M. Perez-Victoria, Comput. Phys. Commun. **118**, 153 (1999).
[48] T. Hahn, in *5th International Symposium on Radiative Corrections (RADCOR 2000)*, Vol. 89 (2000), pp. 231–236, arXiv:hep-ph/0005029.